Mon. Not. R. Astron. Soc. **378,** 189–197 (2007) doi:10.1111/j.1365-2966.2007.11761.x

The effect of dust on Tremaine–Weinberg measurements

Joris Gerssen[1]★ and Victor P. Debattista[2]†
[1]*Astrophysical Institute Potsdam, Potsdam D-14482, Germany*
[2]*Astronomy Department, University of Washington, Box 351580, Seattle, WA 98195, USA*

Accepted 2007 March 20. Received 2007 March 12; in original form 2006 July 28

ABSTRACT

We investigate the effect of dust on the observed rotation rate of a stellar bar. The only direct way to measure this quantity relies on the Tremaine & Weinberg (TW) method which requires that the tracer satisfies the continuity equation. Thus, it has been applied largely to early-type barred galaxies. We show using numerical simulations of barred galaxies that dust attenuation factors typically found in these systems change the observed bar pattern speed by 20–40 per cent. We also address the effect of star formation on the TW method and find that it does not change the results significantly. The results presented here suggest that applications of the TW method can be extended to include barred galaxies covering the full range of Hubble type.

Key words: methods: observational – galaxies: fundamental parameters – galaxies: kinematics and dynamics.

1 INTRODUCTION

The rate at which a bar rotates, its pattern speed, Ω_p, is the principal parameter controlling a barred (SB) galaxy's dynamics and morphology. Most determinations of this parameter are indirect. An often-used method is to match hydrodynamical simulations of SB galaxies to observed velocity fields (see e.g. Weiner, Sellwood & Williams 2001; Pérez, Fux & Freeman 2004; Rautiainen, Salo & Laurikainen 2005, for recent examples). Another commonly used method is to identify morphological features, such as rings, with resonance radii to infer the pattern speed.

The only direct and model-independent technique to measure Ω_p is the Tremaine & Weinberg (1984, hereafter TW) method. They show that if a tracer satisfies the continuity equation, then it is straightforward to derive an expression that relates Ω_p to the luminosity-weighted mean velocity, $\mathcal{V}$, and the luminosity-weighted mean position, $\mathcal{X}$, of this tracer. Gas is generally not a suitable tracer because it is easily shocked, changes states or is converted into stars (e.g. Hernandez et al. 2005; see also Rand & Wallin 2004). The assumption underlying the TW method, that the observed intensity is proportional to the tracer's density, limits its use to relatively dust- and gas-free systems, i.e. early-type galaxies. The model-dependent techniques, on the other hand, rely on the presence of gas and are therefore restricted to late-type barred galaxies. There is therefore no overlapping range in the Hubble type where both methods have been applied and compared.

The number of successful applications of the TW method was initially rather limited: NGC 936 (Kent 1987; Merrifield & Kuijken 1995), NGC 4596 (Gerssen, Kuijken & Merrifield 1999), NGC 1023 (Debattista, Corsini & Aguerri 2002). More recently, larger samples have been obtained: Aguerri, Debattista & Corsini (2002) present a study of five SB0 galaxies and Gerssen, Kuijken & Merrifield (2003) study four early-type barred galaxies. The first successful application of the method using integral field (Fabry–Perot) absorption-line spectroscopy was presented by Debattista & Williams (2004) for NGC 7079, while the first direct detection of the kinematic decoupling in a double-barred galaxy, NGC 2950, using the TW method was presented by Corsini, Debattista & Aguerri (2003). A surprising result emerging from these studies is that bars rotate as fast as they physically can (see also Rautiainen et al. 2005).

Studies of dust extinction in disc galaxies have a long and checkered history (e.g. Holwerda et al. 2005, and references therein). In this paper, we seek to quantify the effect of dust absorption on the TW method. To that end, we will use the *N*-body simulations of barred galaxies by Debattista (2003) (hereafter D03) and Debattista et al. (2006) and implement dust extinction by adjusting the weights of individual particles. Our motivation for this study is to explore how important dust is for TW measurements of both early- and especially late-type galaxies. In the latter, star formation can be a potential problem as it violates the basic assumption of the TW method. We therefore also explore the ability to measure Ω_p in a hydrodynamical simulation of a barred galaxy that includes star formation (SF) (Debattista et al. 2006).

Barred galaxies often display prominent dust lanes along the leading edges of the bar. Numerical simulations associate the dust lanes with shocks in the gas streaming along the length of the bar (Athanassoula 1992). Observations of velocity jumps across dust lanes, as well as the detection of dust lanes in radio continuum, confirm this interpretation (e.g. Mundell & Shone 1999). With the introduction of efficient spectrometers operating in the infrared (IR), the possibility now exists to carry out TW measurements in late-type galaxies, eliminating an important observational bias. We therefore

★E-mail: jgerssen@aip.de
†Brooks Prize Fellow.

test whether such measurements would be compromised by dust extinction and star formation.

Our results show that dust lanes on the leading edges of a bar change the TW derived value of Ω_p depending on the geometry of the observations. This can lead to measured pattern speeds that differ by 40 per cent or less from their true value for realistic dust lane models. As this change can be rather small and because the extinction can be observationally estimated, it suggests that the TW method can be applied to the full range of Hubble type.

This paper is organized as follows. We summarize the TW method and describe the models to which we apply it in Sections 2 and 3, respectively. In Section 4, we describe our models for the dust lane and the diffuse dust disc. The model predictions are presented in Section 5, and in Section 6 we compare the models to data and discuss the implications of our modelling.

2 TW METHOD

For any tracer population that satisfies the condition of continuity, it can be shown that

$$\mathcal{V} = \mathcal{X}\Omega_p \sin i. \quad (1)$$

Here, $\mathcal{X} \equiv \int h(Y) X \Sigma \, dX \, dY$ and $\mathcal{V} \equiv \int h(Y) V_{los} \Sigma \, dX \, dY$ are luminosity-weighted positions and velocities, respectively. The surface brightness of the tracer population is Σ, and V_{los} is the line-of-sight velocity minus the systemic velocity. The galaxy's inclination is given by i and coordinates along its major and minor (disc) axes by (X, Y). The weighting function, $h(Y)$, can be chosen arbitrarily (TW). For several slit observations [i.e. $h(Y) \propto \delta(Y - Y_{offset})$], plotting $\mathcal{V}$ versus $\mathcal{X}$ produces a straight line with slope $\Omega_p \sin i$. In our experiments, we will refer to the slopes obtained from fitting such straight lines as $\Omega \sin i$ in order to distinguish from the intrinsic pattern speed Ω_p obtained from the time evolution.

We apply the TW method to the *N*-body models of barred galaxies described in Section 3 as done by D03. In our measurements, except where noted, we set the inclination $i = 45^\circ$ and the projected angle between the bar major axis and disc major axis, $PA_{bar} = 45^\circ$, implying an intrinsic angle of 54.°7, which is a favourable orientation for the TW method.

As in D03, we use 11 slits each with a width of 0.1 (initial) disc scalelengths (the units of the simulation are described in Debattista et al. 2006) to derive Ω. Tests with slits half and twice as wide return nearly identical results. Applications of the TW method to real data generally use between three and five long-slit spectra. (Integral field observations could soon change this.) A typical observational setup places one slit on the major axis and two slits on opposite sides either near the bar edges or at half the bar radius. Tests with such configurations in the simulations did not yield values of Ω that were significantly different from the results derived with all 11 slits. The strongest constraints on the slope come from slits located about half a bar radius from the galaxy centre. The leverage on the slope of the fit derived from spectra beyond this point is decreasing with radius, as is their signal-to-noise ratio (S/N) (cf. D03). Progressively removing pairs of the outermost slits from the set of 11 and repeating the measurements have little effect on Ω, although it increases the scatter.

3 BARRED GALAXY MODELS

In their study of the effect dust has on the observed kinematics of discs, Baes et al. (2003) used analytical distribution functions for the intrinsic stellar kinematics. However, such methods are ill suited for modelling barred galaxies. In this paper, we explore the effect of dust on barred systems using *N*-body and *N*-body+SPH models.

3.1 *N*-body models

Our four *N*-body simulations TW1–TW4 were evolved on a polar cylindrical grid code (Sellwood & Valluri 1997). The radial spacing of grid cells in this code increases logarithmically from the centre and reaches to well past the edge of the model discs. We used Fourier terms up to $m = 8$ in the potential, which was softened with the standard Plummer kernel. Time integration was performed with a leapfrog integrator using a fixed time-step.

These models use rigid haloes; this allowed us to sample the disc (and bulge, if present) component at high-mass resolution. A full description of these models can be found in D03 and Debattista et al. (2006). Briefly, the rigid haloes were represented either by a spherical logarithmic potential or by a Hernquist halo. In all models, disc kinematics were set up using the epicyclic approximation to give a constant Toomre Q. We assume that all the late-type models are bulgeless and only include a bulge component (using the method of Prendergast & Tomer 1970) in the early-type model presented in D03. We use units in which the initial radial scalelength of the disc particle distribution is 1; in Models TW1–TW4 the vertical scaleheight is then 0.1 in these units. Except where noted, we report results using these natural units. The resulting axisymmetric systems all formed rapidly rotating bars.

Model TW5 is an unpublished simulation with an exponential disc + dominant live dark matter halo evolved with PKDGRAV. Because the halo was live and dominant in this simulation, the bar ends well inside its corotation radius, i.e. it is a slow bar (Debattista & Sellwood 1998; Debattista & Selwood 2000). This also causes the bar to be larger and stronger than any of the others.

3.2 *N*-body+SPH

In late-type galaxies, the rate of SF can be substantial. Thus, stars violate the required condition of (source-free) continuity. To quantify the influence of SF, we also include an *N*-body+SPH model of a barred galaxy in our analysis. This model, described in detail in Debattista et al. (2006), included a live halo and was evolved using a tree code (GASOLINE). The star formation recipe is the one of Katz (1992). In our model, the SF is most pronounced in the central regions of the system and in the bar itself, consistent with numerous observational results (e.g. Sheth et al. 2002).

We measured Ω_p directly from the time evolution; since the dark matter haloes in these models are rigid, Ω_p remained constant after an early phase of evolution. Table 1 lists the properties of the bars, including the pattern speeds Ω_p, of all the models.

3.3 Individual models

The models were selected to have a variety of morphologies and pattern speeds. We generally selected late times in the simulations to ensure that the models are well settled. Here, we use model units.

TW1. This model of an early-type galaxy was described in D03, who used it to study the effect of position angle errors on TW measurements. We use the model at $t = 2.48$ Gyr, by which time a strong and stable bar had formed. Only weak spirals are present in this model, resulting in a minimal interference with the determination of Ω_p. This model has 4×10^6 equal-mass particles in bulge+disc.

Table 1. Our numerical models have bar semimajor axis a_B. The values of a_B were estimated by eye. We measured the pattern speed, Ω_p, from the time evolution. To obtain the dust-free TW method values, Ω_0, we orientated the models to $i = 45^\circ$ and projected $PA_{bar} = 45^\circ$. The difference between Ω_p and Ω_0 is listed under column 'Error'.

Run	a_B (kpc)	Ω_p (km s^{-1} kpc^{-1})	Ω_0 (km s^{-1} kpc^{-1})	Error	Reference
TW1	4.5	23.3 ± 0.8	26.5 ± 0.8	+14 per cent	D03
TW2	7.8	15.0 ± 0.2	15.9 ± 0.1	+6 per cent	Debattista et al. (2006)
TW3	3.8	22.8 ± 0.2	24.2 ± 0.2	+6 per cent	Debattista et al. (2006)
TW4	3.3	34.6 ± 1.1	38.0 ± 4.7	+10 per cent	Debattista et al. (2006)
TW5	8.0	8.8 ± 0.4	9.5 ± 0.5	+8 per cent	unpublished
TW6	5.9	26.4 ± 0.2	25.3 ± 1.1	−4 per cent	Debattista et al. (2006)

TW2. The evolution of this model is discussed in Debattista et al. (2006), where it is referred to as Model L5. We use Model TW2 at $t = 7.44$ Gyr at which time its spiral is relatively weak. It is a late-type model with 7.5×10^6 particles.

TW3. Model TW3 is described in Debattista et al. (2006), where it is referred to as Model H2, and in Debattista et al. (2005), where it is referred to as R7. We use $t = 2.48$ Gyr at which time spirals are rather weak. This late-type model has 4×10^6 particles.

TW4. This late-type model is described in Debattista et al. (2006) where it is referred to as Model S1. We use Model TW5 at an early time, $t = 1.24$ Gyr, when the spiral arms were prominent. This model contains 7.5×10^6 particles.

TW5. Slow bar model, with 0.75×10^6 particles in the disc and 2×10^6 in the halo. We use this model at $t \sim 10.8$ Gyr. Unlike the other models, TW5 is not yet published.

TW6. This model includes SF. It is described in Debattista et al. (2006) where it is referred to as NG3. We use this model at $t = 3.48$ Gyr. At this time, the model contains 0.7×10^6 particles.

4 DUST MODELS

Observations of dust in disc galaxies show that the dust distribution in these systems follows a double-exponential profile (Wainscoat, Freeman & Hyland 1989) and it is conventional to model them as such (e.g. Baes et al. 2003; Valotto & Giovanelli 2004 hereafter VG04). Thus, we model diffuse dust discs as

$$D_{\rm disc}(R, z) = D_{0,\rm disc}\, {\rm e}^{-R/h_{R,\rm disc}}\, {\rm e}^{-|z|/h_{z,\rm disc}}, \quad (2)$$

where $h_{R,\rm disc}$ and $h_{z,\rm disc}$ are the radial scalelength and the vertical scaleheight of the dust disc, respectively. The central dust density is given by $D_{0,\rm disc}$.

4.1 Dust lanes

Late-type barred galaxies often exhibit prominent dust lanes running from the end of the bar toward the centre of the galaxy. Athanassoula (1992) notes that these dust lanes generally fall in two categories: (i) straight dust lanes which are parallel to each other but make an angle with the bar major axis and (ii) curved dust lanes which are parallel to the bar major axis but offset toward the leading edges and with their concave side facing the bar major axis. We implemented both morphologies in our experiments. Since the results obtained with the curved dust lane morphology and the straight dust lane morphology are qualitatively and quantitatively similar, we concentrate only on the latter in this paper.

We implement dust lanes by defining rectangular areas on the bar's leading edges that mimic Athanassoula's straight dust lanes. The dust lane geometry is fully specified by four parameters: the width of the dust lane ($w_{\rm dl}$), the angle the dust lane makes with the bar major axis ($s_{\rm dl}$) and the minimum and maximum extent of the dust lane ($x_{\rm min}$ and $x_{\rm max}$, respectively) along the x (bar) axis. In practice, we fixed $x_{\rm max}$ to the radius of the bar and the dust lanes start on the bar's major axis. A sketch of these various parameters is shown in the left-hand panel of Fig. 1. Note that $x_{\rm min}$ can be negative, i.e. the dust lanes can extend past the centre of the bar. In

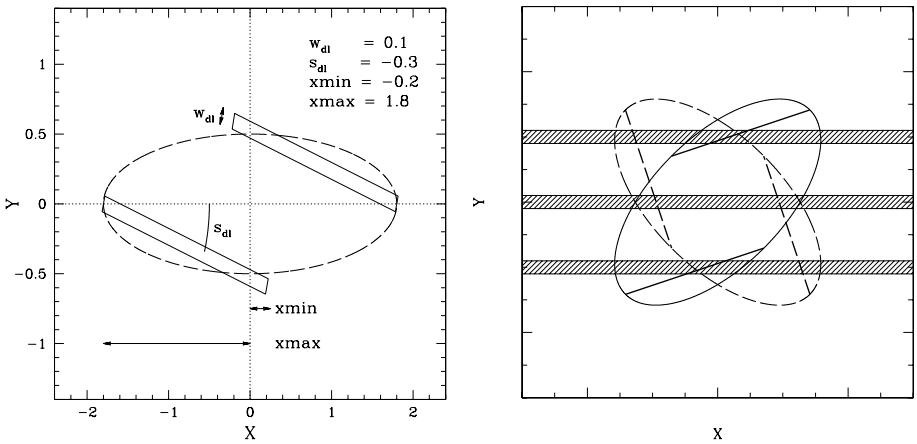

Figure 1. Left-hand panel schematically illustrates the straight dust lane geometry (cf. fig. 1 in Athanassoula 1992) used in our numerical experiments. The bar is represented by the dashed ellipse in this sketch. Right-hand panel: this figure shows that TW measurements of the bar at a positive PA (solid lines) are not equivalent to the same observations at a negative PA (dashed lines). This is because the long slits (hatched areas) intersect the dust lanes, represented by the straight line segments, at different locations depending on the sign of the bar position angle, which leads to a change in sign of the error in Ω.

this case, the inner parts of the dust lanes are sometimes observed to wind around the bulge (see Athanassoula 1992). The sign of PA_{bar} is important, as illustrated in the right-hand panel of Fig. 1, because the slits used to measure the TW integrals intersect the dust lanes at different locations for positive and negative PA_{bar}.

We assume that the dust distribution within the dust lanes can also be described by a double-exponential model:

$$D_{\rm lane}(R,z) = \begin{cases} D_{0,\rm lane}\ {\rm e}^{-R/h_{R,\rm lane}}\ {\rm e}^{-|z|/h_{z,\rm lane}} & \text{if in dust lane,} \\ 0 & \text{otherwise.} \end{cases} \quad (3)$$

Although the dust lane model has a similar double-exponential profile as the dust disc model, the scale parameters of the two components will in general be different.

4.2 Particle weights

In a particle implementation of the TW method, the integrals in equation (1) are replaced by sums over particles. Each particle has its own weight, w. In the collisionless N-body models (TW1 to TW5), all particles are coeval and have equal mass. We therefore assign the same intrinsic (i.e. before applying dust attenuation) weights to all particles in these models.

In Model TW6, however, the particle luminosities, and hence their weights, will depend on their age. To account for this, we scale the intrinsic weights of all particles by their mass-to-light ratio (M/L) ratio in this model. We do not a priori know the luminosity of a particle. We only know its mass $M_{\rm p}$ and time of creation $t_{\rm p}$. To calculate the luminosity of a particle, we follow the procedure first described by Tinsley (1973, see also van der Kruit 1989) and summarized in the Appendix.

When dust is present, particles obscured by dust contribute to the integrals with lower weights. Unlike a foreground screen model, the dust extinction in our models varies with position within the disc. For each particle, we calculate the amount of intervening dust by integrating the projected dust distribution along the line-of-sight. The weight for each particle is then given by $w_i = {\rm e}^{-\tau_i}$, where the optical depth τ_i is obtained from

$$\tau_i = \int_{-\infty}^{s_i} D(s')\,{\rm d}s', \quad (4)$$

assuming a unit mass absorption coefficient. This integral is evaluated using a Gauss–Legendre 64-point quadrature formula from the FORTRAN NAG libraries. To guard against numerically unstable solutions, we subdivided the integration interval into 10 subintervals to improve the accuracy. Examples of the weight distribution in each of our six models are shown in Fig. 2. They are shown here face-on to better illustrate their morphological features.

Following convention, we specify the amount of extinction in our models as the face-on optical depth for a particle infinitely far behind the disc, τ_0. For the dust disc models, we place this particle behind the centre of the disc, while for the dust lanes we place it at a point halfway along the dust lane. Equivalently, the extinction can be expressed in A_V magnitudes

$$A_V = 2.5 \log_{10} e\ \tau_0 = 1.086\tau_0. \quad (5)$$

4.3 Code test: A dust disc

VG04 presented an analytical model of a diffuse dust disc and used this model to demonstrate that the presence of dust lowers the slope of the observed inner rotation curve at large inclinations. As a test of our dust extinction code, we reproduce their result using a simple axisymmetric double-exponential model of a cold rotating disc with $R_{\rm d} = 1.0$ and $z_{\rm d} = 0.1$, respectively. The circular velocities are implemented using equation (2) of VG04 and their 'luminosity class 1' parameters. We sample this model randomly by 10^6 particles. Dust in this model is described by a diffuse disc with geometric parameters that are identical to those for the particle distribution: $h_{R,\rm disc} = R_{\rm d}$ and $h_{z,\rm disc} = z_{\rm d}$. In order to facilitate a direct comparison with the results of VG04, we use the same dust extinction in the disc ($\tau_0 = 3.0$) as they do in their fig. 1(a).

We measured the rotation curves in our model by radially binning the particle velocities in a slit along the major axis. In each radial bin, the line-of-sight velocity distribution (LOSVD) of the particles has a sharp cut-off at high velocities and a tail toward lower velocities. We take the cut-off velocity as the measure of the circular velocity in each bin. The resulting rotation curves are shown in Fig. 3. As these curves are derived from a finite number of particles, they are not as smooth as the analytical results of VG04, but their qualitative and quantitative behaviour is quite similar: internal extinction decreases the slope of the inner rotation curves. This agreement with the results of VG04 strengthens our confidence in our extinction code.

5 RESULTS

The TW-measured value of the bar pattern speed, Ω, can be affected not just by dust but also by spiral structure. We quantify the effect of dust using the ratio Ω/Ω_0, where Ω_0 is the TW-measured value in the absence of dust. To quantify the effect of spirals, we compare Ω_0 with $\Omega_{\rm p}$, the pattern speed inferred from the time evolution of the models, in the absence of dust. The resulting values of Ω_0 for each N-body model are listed in Table 1 and compared to $\Omega_{\rm p}$. The TW measurements generally differ from the time evolution values by $\lesssim$15 per cent (as already noted by D03). Model TW5 included strong spirals in the disc; despite this, Ω differs from $\Omega_{\rm p}$ by less than 10 per cent.

We conclude that in the presence of a strong bar, spirals only perturb TW measurements rather weakly. This is presumably because spirals are at large radius and therefore in lower density parts of the disc. Moreover, because spirals wind around the galaxy centre, their contribution to any slit partly cancels out. Therefore, spirals are not expected to present a serious problem for TW measurements in late-type galaxies with strong bars. (But note that, other than obscuration, we give all particles equal weight; in a real spiral star formation would increase its relative contribution in blue bands.) In the remainder of this paper, we will compare the measurements with and without dust directly, rather than with the time evolution value.

5.1 Diffuse dust disc

We first briefly consider the effect on Ω of a diffuse dust disc. We examined the ratio Ω/Ω_0 resulting from varying the parameter $D_{0,\rm disc}$, and therefore A_V. Typically observed values for A_V range from 0.5 to 4.0 mag (Holwerda et al. 2005). The change in Ω is only 5 per cent for $A_V \sim 3$. Even at $A_V = 8$, the change is less than 15 per cent. We also examined the dependence on the assumed $h_{R,\rm disc}$ and $h_{z,\rm disc}$ of the dust disc at a constant $\tau_0 = 5$. Unsurprisingly, the value of Ω/Ω_0 depends only weakly on either scale parameter at fixed τ_0 once they become of the order of, or larger than, the scale of the stellar system itself. Even for $\tau_0 = 5$, the error in Ω does not exceed 10 per cent.

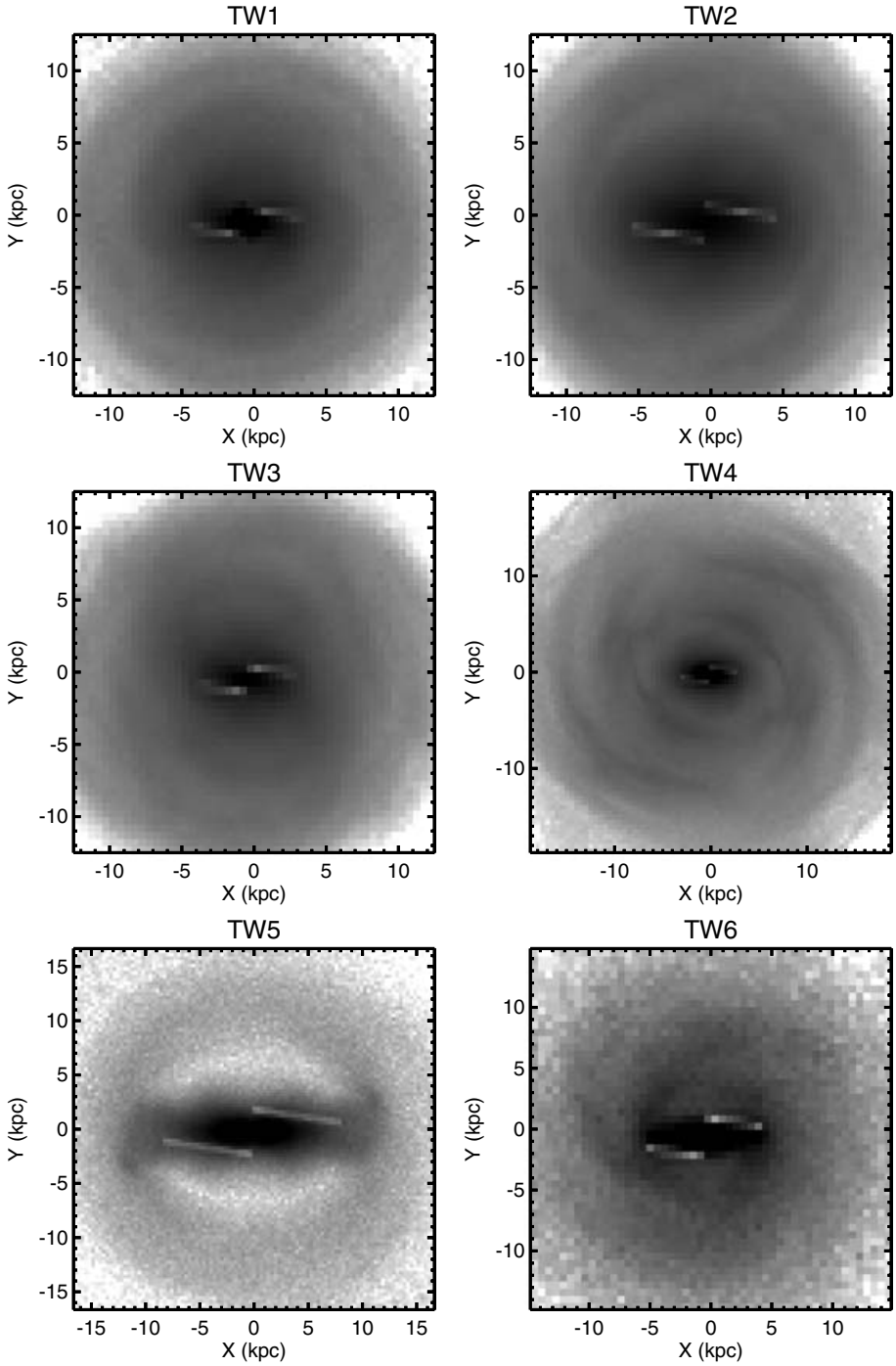

Figure 2. Examples of the projected distribution of particle weights in our numerical models shown on a logarithmic stretch. The models are shown here face-on to highlight their morphological features. Dust lanes have been included to illustrate how dust attenuation is implemented in our simulations. For clarity, the dust lanes have an exaggerated extinction ($A_V = 15$) and width.

In real galaxies, dust within the bar radius is likely to be swept into a dust lane. To simulate this, we tested what the effect of a diffuse dust disc with a hole within the bar radius is (cf Marshall et al. 2006). We set $h_{R,\mathrm{disc}} = 10$, $h_{z,\mathrm{disc}} = 0.1$ and $\tau_0 = 10$. As intuitively obvious, such a dust disc has a negligible (<2 per cent) effect on Ω.

Diffuse dust discs lead to small errors in Ω, of the order of 10 per cent. Existing TW measurement of early-type barred galaxies that lack dust lanes but possibly have diffuse dust discs is therefore unlikely to have been affected substantially by dust. All bars with TW measurements so far are consistent with being fast, in the sense that they end near their corotation radius. This finding supports low dark matter densities at the centres of galaxies (Debattista & Sellwood 1998; Sellwood & Debattista 2006).

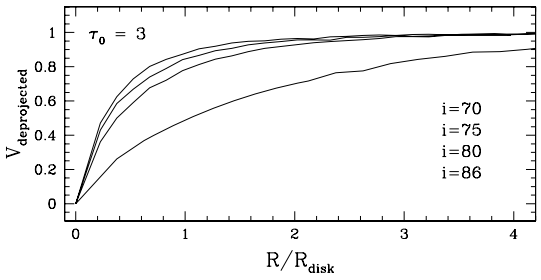

Figure 3. To test our dust code, we reproduce the analytical results of VG04 and derive the major axis rotation curves in an axisymmetric particle data set. We added a diffuse dust disc with a face-on central optical depth of $\tau_0 = 3.0$ and derive the rotation curve at various inclinations. The projected amount of dust extinction varies with inclination leading to more slowly rising rotation curves. From top to bottom, the inclination of the rotation curves varies between 70° and 86°. At the largest inclination, the rotation curve does not reach its asymptotic values before the edge of the *N*-body data (cf. fig. 1a of VG04).

5.2 Dust lanes

We therefore ignore the dust disc contribution in our dust lane models and start by exploring the dust lane geometry and the dust parameters using Model TW1. This is a strongly barred model. As strongly barred galaxies are observed to have flat surface brightness profiles along their major axis (Elmegreen et al. 1996), we set $h_{R,\mathrm{lane}} = 10$ to obtain a nearly constant radial dust lane distribution. For the vertical scaleheight of the dust lane, we set a value of $h_{z,\mathrm{lane}} = 0.1$, which is comparable to the initial stellar distribution.

Using this distribution for the dust lane and $D_{0,\mathrm{lane}} = 100$ (corresponding to an extinction of $A_V \sim 8$), we evaluate the ratio Ω/Ω_0 for varying s_{dl}, w_{dl} and x_{min}. The solid lines in the left-hand panel of Fig. 4 illustrate the variation in this ratio as a function of w_{dl} and x_{min} for constant $s_{\mathrm{dl}} = -0.3$. For all combinations of parameters, the derived ratio is larger than one. Dust lanes therefore lead the TW method to overestimate the pattern speed by 10 to 40 per cent. Variations in the width have the largest impact on Ω as they affect the geometric area of a dust lane the most.

As noted in Section 4.1, the (observationally known) sign of $\mathrm{PA_{bar}}$ is important for the dust lane model. We illustrate this in the same panel using dashed contours for $\mathrm{PA_{bar}} = -45°$. The effect of a negative PA is that Ω becomes smaller than Ω_0 rather than larger as it does for positive PA. Dust lanes can thus also lead the TW method to underestimate the pattern speed. For realistic values of the model parameters (e.g. the NGC 4123 values marked by the cross, see also Section 6), the percentage change in Ω/Ω_0 is roughly independent of the sign of $\mathrm{PA_{bar}}$.

We repeated the exercise for a range of dust lane slopes bracketed by $-0.4 \leqslant s_{\mathrm{dl}} \leqslant -0.1$. The behaviour of Ω/Ω_0 is qualitatively and quantitatively similar for all but the most shallow slope. When $s_{\mathrm{dl}} = -0.1$, the errors in Ω are rather small. This happens because the dust lane is no longer near the leading edge of the bar but closer to the bar major axis. However, $s_{\mathrm{dl}} = -0.1$ bears little resemblance to realistic dust lanes. For most combinations of the dust lane geometry parameters, the observed change is $\lesssim$25 per cent.

5.2.1 *Viewing parameters*

Inclinations of ∼45° and projected angular separations between the bar major axis and the disc major axis of ∼45°, such as we used thus far, are favourable orientations for TW measurements. In the central panel of Fig. 4, we examine the variation in Ω/Ω_0 as a function of inclination and bar position angle. (The dust lane parameters used in this calculation are $x_{\mathrm{min}} = -0.1$, $w_{\mathrm{dl}} = 0.1$ relative to the bar semimajor axis and $s_{\mathrm{dl}} = -0.3$, which correspond to the approximate values observed in the SBc galaxy NGC 4123 scaled to our model.) The error in Ω reaches a maximum when the bar is close to the minor axis at extremely low or high inclinations. Galaxies with such orientations are not usually selected for TW measurements: at large inclinations the projected disc on the sky is too narrow to employ the multiple parallel long slits required by the TW method while at low inclinations the observed velocities, $V_{\mathrm{int}} \sin i$, will generally be too small to measure reliably. Around $i = 45°$ and $\mathrm{PA_{bar}} = 45°$, the results are independent of bar position angle and depend only weakly on inclination. For $30° < i < 60°$ and $20° < \mathrm{PA_{bar}} < 80°$, these errors are less than 25 per cent.

5.2.2 *Scalelength parameters*

The observed pattern speed depends only weakly on variations in $h_{R,\mathrm{lane}}$. As our initial $h_{R,\mathrm{lane}}$ is 10 times that of the particle distribution, even large variations around this initial value do not lead to significant changes in Ω. The dependence on $h_{z,\mathrm{lane}}$ is somewhat stronger as illustrated in the right-hand panel of Fig. 4. Once

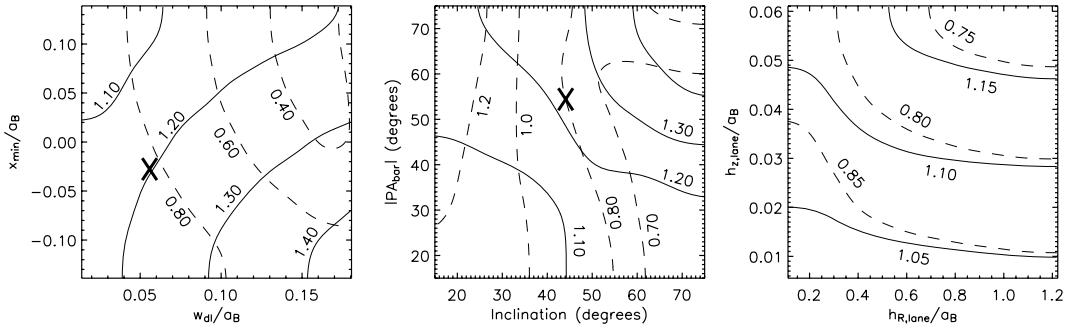

Figure 4. Illustrations of the effect of varying the *dust lane* model on Ω. The contours show the ratio Ω/Ω_0. In each panel, we evaluate this ratio at a fixed value of the extinction ($A_V \sim 8$) and with a dust lane slope of $s_{\mathrm{dl}} = -0.3$. Unlike the axisymmetric *dust disc* model, the sign of $\mathrm{PA_{bar}}$ matters (see Fig. 1). The plotted contours are for $\mathrm{PA_{bar}} = +45°$ (solid) and $\mathrm{PA_{bar}} = -45°$ (dashed). Left-hand panel: the ratio Ω/Ω_0 for varying dust lane width (w_{dl}) and minimum dust lane radius (x_{min}). centre: the behaviour of the ratio Ω/Ω_0 as a function of viewing parameters. In this panel, the dust lane model parameters are fixed at $x_{\mathrm{min}} = -0.1$ and $w_{\mathrm{dl}} = 0.1$. right-hand panel: the dependence of the ratio on the scalelength parameters of the dust lane model. For reference, the initial scalelengths of the disc particle distribution are $R_{\mathrm{d}} = 1.0$ and $z_{\mathrm{d}} = 0.1$. The cross in the left-hand and middle panels marks the approximate location of NGC 4123 in these panel (see Section 6 but note that the extinction in NGC 4123 is only $A_V \simeq 3$).

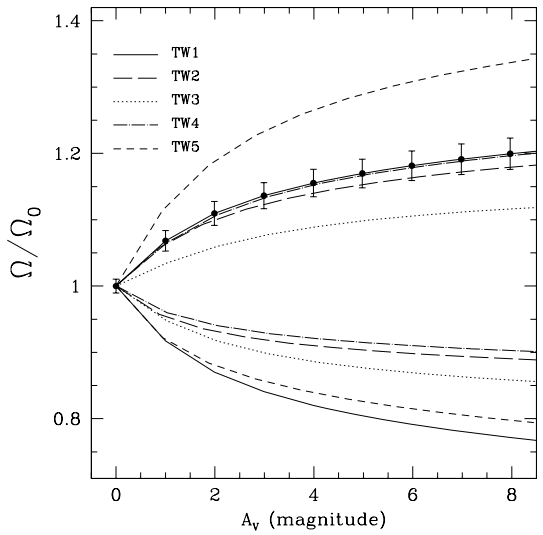

Figure 5. The ratio Ω/Ω_0 of the bar pattern speed observed with the TW method to the intrinsic bar pattern speed as a function of dust lane extinction A_V (defined face-on as described in Section 4.2). The different curves show the behaviour of this ratio for the different *N*-body models. Two curves are shown for each model. Curves with a ratio >1 are at $\mathrm{PA_{bar}} = +45^\circ$, while curves with a ratio <1 are at $\mathrm{PA_{bar}} = -45^\circ$. The dust lane geometry and dust distribution are the same for every model: $w_{\rm dl}/a_B = 0.1, s_{\rm dl} = -0.3, x_{\rm min}/a_B = -0.1, h_{R,\rm lane} = 10$ and $h_{z,\rm lane} = 0.1$. For clarity, the 1σ errors are shown for Model TW1 only.

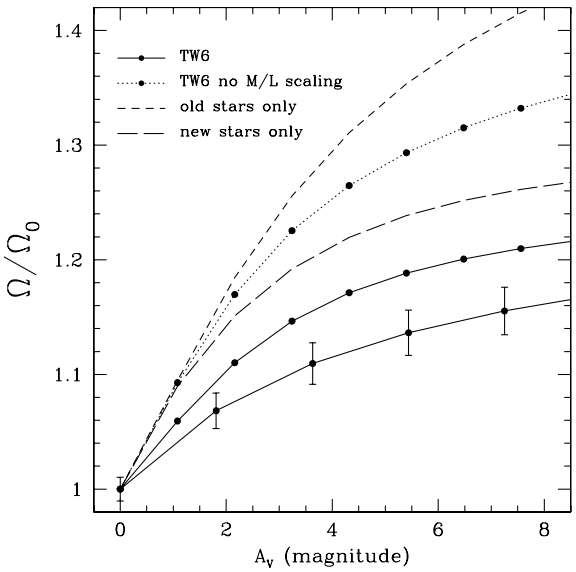

Figure 6. The ratio Ω/Ω_0 as a function of dust extinction for the model that includes SF (TW6). The result is not very different from the models shown in Fig. 5. For comparison, Model TW1 is overplotted as the solid line with error bars. Without M/L scaling (see text), dust affects Model TW6 significantly more than our previous models. The other curves show the behaviour of Ω in TW6 for particle subsets in age. The younger the particles the less the effect of dust appears to be.

$h_{R,\rm lane}$ or $h_{z,\rm lane}$ becomes larger than the corresponding quantities for the stellar distribution, Ω/Ω_0 becomes independent of these parameters.

5.3 Different *N*-body models

In the previous sections, we explored the behaviour of Ω on the dust model parameters with only Model TW1, largely to facilitate comparisons with D03, who used the same model. We carried out a similar parameter space study for all the other *N*-body models presented in Section 3. The same dust lane geometry (with $x_{\rm min}$ and $w_{\rm dl}$ rescaled to a_B) and dust distribution used in Section 5.2 were used on each *N*-body model. Only the maximum radii of the dust lanes ($x_{\rm max}$) differ to account for the different bar lengths in each model (see Table 1). The dust lane widths used here are fairly narrow, about 5 per cent of the bar semimajor axis length, to resemble the shapes of observed dust lanes. These yield qualitatively similar results. A quantitative comparison of the different *N*-body models is shown in Fig. 5 where the ratio Ω/Ω_0 as a function of extinction is plotted for each model. The main difference is in the errors in Model TW5 at positive $\mathrm{PA_{bar}}$: the error for this slow bar is a factor of 2 larger than in the other models. However, at negative $\mathrm{PA_{bar}}$ the error in this model is not much different than the other models.

5.4 Star formation

The models that we explored so far do not take SF into account. However, in late-type systems the SF rate can be large enough that departures from continuity become too large. Bright young stars will contribute disproportionately to the TW integrals $\mathcal{X}$ and $\mathcal{V}$ (see Section 2) and hence may significantly change the measured pattern speed. To quantify the effect of star formation on the TW method, we use Model TW6. The result is shown in Fig. 6 and is qualitatively similar to the results derived from Models TW1 to TW5. Quantitatively, the impact of dust in TW6 lies between the values in Models TW1–TW4 and TW5, with an Ω value that differs from its true values (at $A_v = 3$) by 15 per cent. Scaling the intrinsic weights of the particles by their M/L ratio (Section 3.2) is a crucial part of Model TW6. As a test, we therefore derive the pattern speeds in this model without any such scaling (dotted line in Fig. 6). Without this scaling, the effects of dust are comparable to the slow bar model TW5 with Ω deviating from the intrinsic value by 21 per cent.

To examine this more closely, we divided the particles in two groups, those particles that were present in the simulation from $t = 0$ ('old') and the ones that were created subsequently by SF ('new'). The pattern speed derived from younger particles appears to be less affected by dust. In fact, subdivisions into younger ages show even shallower curves. Interestingly, the dust-free values of Ω_0 derived for the different age bins vary by less than 8 per cent from the full model. This may be somewhat fortuitous as there are fewer particles at younger ages to derive the TW value. Their spatial extent is also smaller as these particles are mostly confined to the bar region and the nucleus.

This behaviour is probably due to the similar location of dust lanes and SF regions. If SF occurs or is enhanced on the leading edges of a bar, as is frequently observed, e.g. Sheth et al. (2002), then absorption by dust may be partially mitigated by the enhanced luminosity of the young particles. SF is indeed observed along the bar in this model.

6 DISCUSSION

The experiments presented in this paper show that dust lanes on the leading edges of a bar tend to increase the TW-derived value of the bar pattern speed, Ω, when $\mathrm{PA_{bar}} > 0$ and decrease it when $\mathrm{PA_{bar}} < 0$. The changes in Ω are relatively modest for realistic dust lanes (i.e.

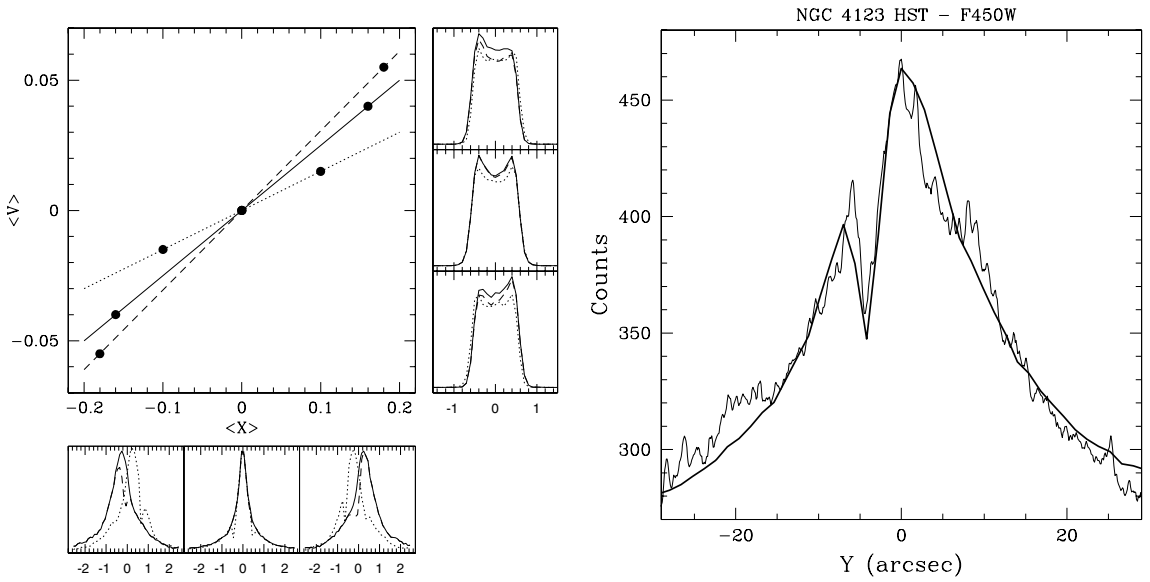

Figure 7. Left-hand side: sketch illustrating the effect of leading edge dust lanes on the derived pattern speed. The solid lines show the results derived from the *N*-body model using three slits in the absence of dust. The dashed lines show the results obtained when leading edge dust lanes are included in a model with $\mathrm{PA_{bar}} = +45^\circ$. The dotted lines show results derived using the same model but with $\mathrm{PA_{bar}} = -45^\circ$. The central panel plots the mean line-of-sight velocities, $\langle V\rangle$ or $\mathcal{V}$, versus the mean position, $\langle X\rangle$ or $\mathcal{X}$, for each slit. The slope of the linear fit gives $\Omega \sin i$. The dust lane modifications to the velocity and luminosity profiles (shown in the sub-panels) lead to either a steeper or a shallower slope of the fit depending on $\mathrm{PA_{bar}}$ (see Fig. 1). The velocity profiles from top to bottom and the luminosity profiles from left- to right-hand side are derived from slits located at $Y = -0.4$, 0.0 and 0.4, where Y is defined as in Fig. 1. Right-hand panel: the ragged line shows a cut across the dust lane in an *HST*-WFPC2 image of NGC 4123 in the F450W filter. To improve the statistics, the profile is summed over 100 pixels ($\sim$10 arcsec or about one-fifth of the bar radius) along the dust lane. The dust lane itself is clearly notable as the depression at $y \approx -5$ arcsec. The smooth bold line shows a similar cut in Model TW1 at a dust lane extinction of $A_V = 3.0$ and is summed over approximately the same fraction of the dust lane. The model profile is scaled in an ad hoc fashion to match the peak of the observed profile. The agreement with the observed profile is remarkably good.

$A_V \lesssim 3$), between 8 and 25 per cent (cf. Figs 5 and 6) and increasing to 20–40 per cent at unrealistically large $A_V \sim 8$ or if the bar is slow. Somewhat surprisingly, the simulation that includes SF (TW6) does not change this conclusion in a significant way. Dust lanes alone therefore pose no serious problem when trying to extend the TW method to late-type barred galaxies.

Fig. 7(a) illustrates why the measured Ω changes when dust lanes are present. Shown by solid lines in this figure are the spatial and velocity profiles along three slits in Model TW1 in the absence of dust. The dashed lines show the same profiles but for a model that includes leading edge dust lanes when $\mathrm{PA_{bar}} = +45^\circ$, while the dotted lines are for $\mathrm{PA_{bar}} = -45^\circ$. The spatial profiles clearly show the asymmetric behaviour expected for this configuration (cf. Fig. 1b). The measured pattern speed Ω follows from the slope of the linear fit to the means of the velocity and spatial profiles. The dust distribution affects both the spatial and the velocity profiles. If dust would alter only the spatial profiles but leave the velocity profiles unchanged then the slope of the linear fit would flatten, leading to slower pattern speed when $\mathrm{PA_{bar}} = +45^\circ$. However, the associated change in $\mathcal{V}$ due to the dust more than offsets this effect and the bar pattern speed therefore appears larger with dust than without.

The bars in Models TW1 to TW4 are classified as 'fast'. That is to say that the ratio of the corotation radius to the bar radius in these models is close to but greater than 1.0. This ratio cannot be smaller than 1.0 as that would violate self-consistency (Contopoulos & Papayannopoulos 1980). Applications of the TW method to real data for early-type galaxies have not revealed slow (i.e. with a ratio $\gtrsim$2) bars. We nevertheless included a slow bar, Model TW5, to examine the effect of dust in such a case. In this model, the impact of dust on Ω is larger than in the fast bars (Fig. 5). This is not surprising as the absolute change in Ω between successive steps in A_v is, to within a factor of 2, independent of the details of a particular model. In other words, the factor by which dust acts to change Ω is similar for all models and hence makes more of an impact on a slow bar. A similar behaviour is observed in Model TW6 (Fig. 6). The ratio of bar radius to corotation radius is about 1.5 indicating that this bar is slowish. The observed pattern speed is indeed more affected by dust than in Models TW1–TW4.

An important concern with TW measurements in late-type systems is the requirement of a well-constrained PA. D03 demonstrates that a PA error of 5° can result in pattern speed errors by up to 100 per cent (see also Debattista & Williams 2004). In real galaxies, non-axisymmetric features can lead to uncertainties in the derived position angles (and inclinations) that are on average 5° (Barnes & Sellwood 2003). It is therefore crucial to select systems with well-constrained PAs when applying the TW method to real late-type galaxies.

Weiner et al. (2001) presented a $B - I$ colour map of the SBc galaxy NGC 4123 that clearly delineates the dust lanes on the leading edges of its bar. They found that $\langle B - I\rangle = 2.3$ in the dust lanes. With the extinction law of Rieke & Lebofsky (1985), this colour implies an average extinction in the dust lanes of $A_V = 2.7$ mag. We checked this value using a *Hubble Space Telescope* (*HST*) archival WFPC2 F450W band image of NGC 4123 (SNAP-9042 PI: Smartt) to compare a surface brightness profile across the dust lane (i.e. parallel to the bar minor axis) in the *HST* image to a similarly placed slit in Model TW1. We use $A_V = 3$ to match the value implied by the Weiner et al. (2001) colour map. As the exposure time of the *HST* image is only 160 s, we increase the S/N of the surface brightness cut by summing over 100 pixels along the dust lane. This corresponds to a length of about 10 arcsec over the dust lane or a fifth of the bar radius (Weiner et al. 2001). The ragged line in Fig. 7(b) shows the

resulting surface brightness profile. The dust lane itself is clearly notable as the depression near $y \approx -5$ arcsec. The smooth bold line represents a similar cut along the model image averaged over a similar fraction of the dust lane. The model profile is scaled ad hoc to match the peak in the NGC 4123 data: the resulting profile fits the observed one remarkably well. Using this extinction, the models shown in Figs 5 and 6 predict a ∼15 per cent change in the observed bar pattern speed. If, on the other hand, the observations were carried out in K band using the CO band head, the extinction of $A_V = 2.7$ mag translates to $A_K = 0.112$ (e.g. Rieke & Lebofsky 1985, their table 3). This extinction would lead to insignificant errors in Ω from obscuration.

Our results suggest that the application of the TW method can be extended to later-type barred galaxies. We therefore propose that at this time a test case of a TW measurement in a late-type galaxy is warranted. A useful approach would be to try a TW measurement on a bar with pattern speed measured by hydrodynamical modelling (Weiner et al. 2001; Pérez et al. 2004).

ACKNOWLEDGMENTS

VPD is supported by a Brooks Prize Fellowship at the University of Washington and receives partial support from NSF ITR grant PHY-0205413. We would like to thank Rok Roškar for granting us permission to use Model TW5 here ahead of publication. We thank the anonymous referee for comments that helped to improve this paper.

REFERENCES

Aguerri J. A. L., Debattista V. P., Corsini E. M., 2003, MNRAS, 338, 465
Athanassoula L., 1992, MNRAS, 259, 345
Baes M. et al., 2003, MNRAS, 343, 1081
Barnes E. J., Sellwood J. A., 2003, AJ, 125, 1164
Contopoulos G., Papayannopoulos Th., 1980, A&A, 92, 33
Corsini E. M., Debattista V. P., Aguerri J. A. L., 2003, ApJ, 599, L29
Debattista V. P., 2003, MNRAS, 342, 1194 (D03)
Debattista V. P., Sellwood J. A., 1998, ApJ, 493, L5
Debattista V. P., Sellwood J. A., 2000, ApJ, 543, 704
Debattista V. P., Williams T. B., 2004, ApJ, 605, 714
Debattista V. P., Corsini E. M., Aguerri J. A. L., 2002, MNRAS, 332, 65
Debattista V. P., Carollo C. M., Mayer L., Moore B., 2005, ApJ, 628, 678
Debattista V. P., Mayer L., Carollo C. M., Moore B., Wadsley J., Quinn T., 2006, ApJ, 645, 209
Emsellem E., Greusard D., Combes F., Friedli D., Leon S., Pécontal E., Wozniak H., 2001, A&A, 368, 52
Elmegreen B. G., Elmegreen D. M., Chromey F. R., Hasselbacher D. A., Bissell B. A., 1996, AJ, 111, 2233
Gerssen J., Kuijken K., Merrifield M. R., 1999, MNRAS, 306, 926
Gerssen J., Kuijken K., Merrifield M. R., 2003, MNRAS, 345, 261
Hernandez O., Wozniak H., Carignan C., Amram P., Chemin L., Daigle O., 2005, ApJ, 632, 253
Holwerda B. W., Gonzalez R. A., Allen, Ronald J., van der Kruit P. C., 2005, AJ, 129, 1396
Katz N., 1992, ApJ 391, 502
Kent S. M., 1987, AJ, 93, 1062
Marshall D. J., Robin A. C., Reylé C., Schultheis M., Picaud S., 2006, A&A, 453, 635
Merrifield M. R., Kuijken K., 1995, MNRAS, 274, 933
Mundell C. G., Shone D. L., 1999, MNRAS, 304, 475
Pérez I., Fux R., Freeman K., 2004, A&A, 424, 799
Prendergast K. H., Tomer E., 1970, AJ, 75, 674P
Rand R. J., Wallin J. F., 2004, ApJ, 614, 142
Rautiainen P., Salo H., Laurikainen E., 2005, ApJ, 631, 129
Rieke G. H., Lebofsky M. J., 1985, ApJ, 288, 618
Sellwood J. A., Debattista V. P., 2006, ApJ, 639, 868
Sellwood J. A., Valluri M., 1997, MNRAS, 287, 124
Sheth K., Vogel S. N., Regan M. W., Teuben P. J., Harris A. I., Thornley M. D., 2002, AJ, 124, 2581
Silge J. D., Gebhardt K., 2003, AJ, 125, 2809
Tinsley B. M., 1973, ApJ, 186, 35
Tremaine S., Weinberg M. D., 1984, ApJ, 282, L5 (TW)
Valotto C., Giovanelli R., 2004, AJ, 128, 115 (VG04)
van der Kruit P. C., 1989 in Saas-Fee Advanced Course No. 19
Wainscoat R. J., Freeman K. C., Hyland A. R., 1989, ApJ, 337, 163
Weiner B. J., Sellwood J. A., Williams T. B., 2001, ApJ, 546, 931

APPENDIX

We know the mass $M_{\rm p}$ and time of formation $t_{\rm p}$ of all particles in Model TW6. To calculate the luminosity of a particle, we follow Tinsley (1973). We begin by assuming that the stars that make up a particle (typical mass $\sim 10^5\,{\rm M}_\odot$) are distributed according to a Salpeter IMF: $f(M) = CM^{-2.35}$. The number of stars in a particle, C, can be found by setting $M_{\rm tot} \times C = M_{\rm p}$. The total mass is

$$M_{\rm tot} = \int_{M_{\rm lo}}^{M_{\rm up}} f(M)\,{\rm d}M,$$

where $M_{\rm lo} = 0.1\,{\rm M}_\odot$ and $M_{\rm up} = 100\,{\rm M}_\odot$. We can now calculate the total luminosity of this particle by assuming that the luminosity along the main-sequence scales as M^α where $\alpha = -4.1$. Then,

$$L_{\rm tot} = C \int_{M_{\rm lo}}^{M_{\rm up}} M^\alpha M^{-2.35}\,{\rm d}M$$

at the moment the particle is created.

At later times, the more massive stars will have turned off the main sequence. The upper limit for a star on the main sequence is given by $M_{\rm up} = \frac{t_{\rm p}}{10\,{\rm Gyr}}^{1/\gamma}$ where $\gamma = -2.5$. By using this value for $M_{\rm up}$ in the $L_{\rm tot}$ equation, the luminosity of a particle at any time t can be derived. Stars with masses larger than $M_{\rm up}$ go through a luminous but short-lived giant phase. We include the contribution of giants in our calculation of $L_{\rm tot}$ following van der Kruit (1989). But only in the older particles do they make a contribution comparable to the main-sequence stars.

This paper has been typeset from a TEX/LATEX file prepared by the author.